Modeling and simulation of local physical stress on the mastocytes created by the needle manipulation during acupuncture

Yannick Deleuze, Marc Thiriet, Tony W.H. Sheu

Modeling and simulation of local physical stress on the mastocytes created by the needle manipulation during acupuncture

Yannick Deleuze[1,2,*], Marc Thiriet[1,3,4], and Tony W.H. Sheu[2,5]

[1] *Sorbonne Universités, UPMC Univ Paris 06, UMR 7598, Laboratoire Jacques-Louis Lions, F-75005, Paris, France.*
[2] *Department of Engineering Science and Ocean Engineering, National Taiwan University, No. 1, Sec. 4, Roosevelt Road, Taipei, Taiwan.*
[3] *CNRS, UMR 7598, Laboratoire Jacques-Louis Lions, F-75005, Paris, France.*
[4] *INRIA-Paris-Rocquencourt, EPC REO, Domaine de Voluceau, BP105, 78153 Le Chesnay Cedex.*
[5] *Center for Advanced Study in Theoretical Sciences, National Taiwan University, No. 1, Sec. 4, Roosevelt Road, Taipei, Taiwan.*

Abstract. In this paper, we study the effects of inserted needle on the subcutaneous interstitial flow. A goal is to describe the physical stress affecting cells during acupuncture treatment. The model consists of the convective Brinkman equations to describe the flow through a fibrous medium. Numerical studies in FreeFem++ are performed to illustrate the acute physical stress developed by the implantation of a needle that triggers the physiological reactions of acupuncture. We emphasize the importance of numerical experiments for advancing in modeling in acupuncture.

AMS subject classifications: 76M10, 76S05, 76Z05, 92C50

Key words: Finite element method, FreeFem++, acupuncture, Brinkman model, interstitial fluid flow

1 Introduction

Acupuncture is one of the oldest healing practices and alternative medicines. This minimally invasive procedure involves a penetration of skin with needles to stimulate specific points on the body, called acupoints, with the purpose of restoring balance in the flow of *qì* through meridians [1]. While this so-called traditional Chinese medicine has been

---

Corresponding author. Email addresses: yannick.deleuze@ljll.math.upmc.fr (Y. Deleuze), marc.thiriet@upmc.fr (M. Thiriet), twhsheu@ntu.edu.tw (T. W.H. Sheu)

recognized in 2010 on the Representative List of the Intangible Cultural Heritage of Humanity by UNESCO and was endorsed by the World Health Organization, there is a great demand to enlighten its underlying concepts such as *qì*, meridians, and acupoints. The absence of scientific background of acupuncture mechanisms certainly has motivated us to carry out modeling and numerical simulation of both macroscopic and microscopic aspects of the acupuncture process.

The classical technique involves inserting a hair-thin needle into acupoints. The needle is then manipulated to yield a local mechanical stress field through needle motions (lifting–thrusting cycle or rotation). After a short term of needle manipulation, the needle is retained until desired effects have been achieved. The mechanical interaction of needle with the skin and the subcutaneous tissue has been demonstrated [2]. This stimulation via mechanotransduction, that is activated by the stretch of mechanosensitive ion channels at the mastocyte surface, can lead to a cascade of biochemical reactions that drive acupuncture effects [3].

The same acupoint can be stimulated by acupressure, moxibustion, electroacupuncture, and, more recently, by laser acupuncture. Acupressure, or needleless acupuncture, stimulates the acupoints by applying finger pressure near these points that in turn creates a local mechanical stress. Electroacupuncture (or percutaneous electrical nerve stimulation) [4] creates a local electrical field by applying a small electric current between a pair of acupuncture needles at acupoints. Laser acupuncture [5] is an optical method to stimulate acupoints with laser irradiation. Laser acupuncture does not seem to work via physical processes such as excitation with an electromagnetic wave and heating. Laser acupuncture seems to trigger phototransduction pathways.

Moxibustion is a popular alternative TCM therapy that involves burning a mugwort stick (or moxa candle) manipulated back and forth along a short meridian segment centered at a given acupoint. To reduce the risk of burning of skin, indirect moxibustion using both needles and ignited moxa is currently more popular. This practice involves inserting a needle into an acupoint and retaining it for a proper duration. The tip of the needle is then ignited to supply heat flux to the point about acupoint. Moxibustion may trigger opening of thermosensitive ion channel. This motivated our previous studies of the transfer of heat from burning moxa in an indirect moxibustion setting [6–9].

Whatever the operation mode is, calcium entry in the mastocyte triggers degranulation and release of chemoattractants, neural stimulants, and endocrine substances. Such a process is sustained by the recruitment of mastocytes (chemotaxis). We have developed a model of chemotactic self-sustained response of mastocytes [10, 11]. The developed mathematical model constitutes a system of parabolic partial differential equations. Its simplest form describes the evolution of the density of mastocytes and the chemoattractant concentration subjected to a physical stress.

The present study is aimed at simulating the effects of an inserted needle on the interstitial flow. The reader is invited to read the accompanying paper [12] to get information on events occurring during the permanent regime, that is once the needle has been implanted and the stress field in the subcutaneous connective tissue is fully established.

This paper is organized in the following. Section 2 outlines the physiological mechanisms and the biological tissue involved during acupuncture treatment. Section 3 presents the mathematical modeling and the governing equations of flow in interstitium. The ALE finite element method is reviewed in Section 4. Numerical experiments are discused in Section 5. In Section 6, concluding remarks are given.

2   Biological medium

2.1   Connective tissue

The skin consists of three layers of tissue known as the epidermis, dermis, and hypodermis lying above skeletal muscles. The hypodermis, a loose connective tissue, provides (1) structural and mechanical support, (2) transport of nutrients, metabolites, and waste between the blood and tissues, (3) storage of energy, and (4) immunological defense. For a complete description of the extracellular matrix we refer to [13,14].

Like other types of connective tissues, the loose connective tissue is constituted of scattered cells immersed in extracellular matrix. The extracellular matrix contains an abundant ground substance and relatively sparse fibers. The ground substance fills the space between cells and fibers and consists of water, proteoglycans, and other macromolecules, thereby forming a viscous hydrated gel that can stabilize fiber network. Proteoglycans control the level of hydration of connective tissues and thus can partially determine the physical properties of connective tissues.

There is ample evidence that acupoints are located mainly in the hypodermis close to neurovascular bundles [15]. Acupoints differentiate from nonacupoint locations by displaying high density of mastocytes and capillaries, high skin electrical conductance, and high ionic concentrations (K^+, Ca^{++}, Fe^{++}, Mn^{++}, Zn^{++}, PO_4^{3-}).

2.2   The interstitial fluid

The interstitial fluid contains water, ions and other small molecules. Such a fluid corresponds to plasma without macromolecules. It interacts with the ground substance to form a gel-like medium.

A model taking into account individual fibers and cell adhesion complexes is already a falsification of the reality. Moreover, it is very costly from the computational sense. When considering an organized homogeneous matrix of fibers, computation of such a model shows the microscopic fluctuations of the fluid shear stress at the protein level [16].

On a microscopic scale, the interstitial is composed of fluid and solid fibers, thereby clearly forming two phases. Homogeneized two-phase media coupling with a Newtonian fluid and an elastic matrix have been considered to model soft tissue [17]. This well-posed model exhibits both the fluid and the viscoelastic property of the fluid.

The interstitial tissue can be modeled as a porous medium [18]. The Darcy's law approximates fibers of the media as a continuum and allows to compute the actual mi-

croscopic flow phenomena that occur in the fibrous media. The phenomenological model cannot give information on unneeded microscopic events but the Darcy equation can describe macroscale flow patterns in porous media.

The Brinkman equation [19] is an extension of the Darcy equation. Introduction of a second order derivative in the Darcy equation allows the application of no-slip boundary conditions. The Brinkman equation can thus describe the flow field around solid bodies such as the embedded cells in extracellular matrix but the fibrous medium itself, e.g., the individual fibers, is still treated as a continuum.

The interstitial tissue can also be modeled by a poroviscoelastic material [20]. Biot developed a theory of poroelasticity for setting the resistance to flow through deformable fluid-saturated porous media [21–24]. The interstitial fluid, cells, and the extracellular matrix are viewed as a two-phase system consisting of a solid and a fluid phase, each of which is regarded as a continuum. Biot's equations for the linear theory of poroelasticity are derived from the equations of linear elasticity for the solid matrix, the Navier–Stokes equations for the incompressible viscous fluid, and the Darcy's law for the flow of a fluid through fibrous matrix.

In the context of acupuncture, the interstitial flow has been modeled by the Brinkman equations. The flow is driven by the difference in hydrostatic and osmotic pressures between the capillaries and the interstitial space [25, 26].

Interstitial flow and deformed matrix fibers exert directly stress at the cell surface that can be sensed by membrane molecules. Mastocytes, among other cells, respond to fluidic stimuli caused by the fluid shear stress [27]. In this article, the transient convective Brinkman equations are applied to simulate the interstitial flow in a porous medium driven by a moving needle.

3 Mathematical modeling and methods

3.1 Governing equations

In the present work, we study the effects of a moving needle on the interstitial fluid. We then consider a fluid motion governed by the incompressible convective Brinkman equations for a fluid-filled porous material. The Reynolds number and the Darcy number are normally small. As a result, the nonlinear drag such as the Forchheimer law [28] can be neglected. The derivation of the incompressible convective Brinkman equations was given in [29–31] in the context of heat transfer in porous media. The set of equations is as follows:

$$\frac{\rho}{\alpha_f}\left(\frac{\partial \bar{\mathbf{u}}}{\partial t}+\bar{\mathbf{u}}\cdot\boldsymbol{\nabla}\left(\frac{\bar{\mathbf{u}}}{\alpha_f}\right)\right)-\mu\nabla^2\bar{\mathbf{u}}+\frac{1}{\alpha_f}\boldsymbol{\nabla}(\alpha_f p_f)=-\frac{\mu}{\mathcal{P}}\bar{\mathbf{u}}\quad\text{in }\Omega,$$

$$\boldsymbol{\nabla}\cdot\bar{\mathbf{u}}=0\qquad\text{in }\Omega,$$

(3.1)

where $-\frac{\mu}{\mathcal{P}}\bar{\mathbf{u}}$ denotes the Darcy drag, μ the fluid dynamic viscosity, ρ the fluid density, $\mathcal{P}$ the Darcy permeability, $\bar{\mathbf{u}}$ the averaged velocity and p_f the pressure. The averaged

velocity is defined as

$$\bar{\mathbf{u}} = \alpha_f \mathbf{u}_f, \tag{3.2}$$

where $\mathbf{u}_f$ is the fluid velocity and

$$\alpha_f = \frac{\text{fluid volume}}{\text{total volume}} \tag{3.3}$$

is the fluid volume fraction. This volume fraction corresponds to the effective porosity of the medium. The fluid fractional volume α_f is taken as a space-dependent parameter to model the distinguished properties of an acupoint.

The system (3.1), subject to the initial conditions given below, are solved in the domain Ω

$$\bar{\mathbf{u}}(\mathbf{x}, 0) = \bar{\mathbf{u}}_0(\mathbf{x}). \tag{3.4}$$

The domain boundary (figure 1) can be decomposed into the needle boundary denoted by Γ_{needle}, an impervious boundary (wall) denoted by Γ_{wall}, and the open boundary on the sides denoted by Γ_{sides}.

On the top and bottom of the domain Ω, the boundary condition on Γ_{wall} is prescribed as

$$\bar{\mathbf{u}} = 0. \tag{3.5}$$

On the needle boundary Γ_{needle}, the boundary condition is imposed as

$$\bar{\mathbf{u}} = \mathbf{v}_{\text{needle}}. \tag{3.6}$$

On both sides of the domain Ω, the traction-free boundary condition is prescribed on Γ_{sides} as

$$-\mu \boldsymbol{\nabla} \bar{\mathbf{u}} \cdot \mathbf{n} + p_f \mathbf{n} = 0. \tag{3.7}$$

4 Computational model

4.1 Scaling and setting for numerical simulations

L denotes the characteristic length that is the needle width and V the characteristic velocity set to be the needle maximum velocity. Rescaling the variables thereby leads to

$$\mathbf{x}' = \frac{\mathbf{x}}{L}, \quad t' = \frac{t}{(L/V)}, \quad p' = \frac{p_f}{(\rho V^2)}, \quad \mathbf{u}' = \frac{\bar{\mathbf{u}}}{V}. \tag{4.1}$$

In the resulting dimensionless form, after removing the prime in the rescaled variables, the dimensionless incompressible convective Brinkman equations read as

$$\frac{1}{\alpha_f} \frac{\partial \mathbf{u}}{\partial t} + \frac{1}{\alpha_f} \mathbf{u} \cdot \boldsymbol{\nabla} \left(\frac{\mathbf{u}}{\alpha_f} \right) - \frac{1}{\text{Re}} \nabla^2 \mathbf{u} + \frac{1}{\alpha_f} \boldsymbol{\nabla} (\alpha_f p) = -\frac{1}{\text{DaRe}} \mathbf{u}, \tag{4.2}$$

$$\boldsymbol{\nabla} \cdot \mathbf{u} = 0. \tag{4.3}$$

where Re is the Reynolds number and Da is the Darcy number. The two dimensionless parameters are defined as

$$\text{Re} = \frac{\rho LV}{\mu}, \quad \text{Da} = \frac{\mathcal{P}}{L^2}. \tag{4.4}$$

In considering the above dimensionless governing equations, the boundary condition on the domain boundary is prescribed as

$$\mathbf{u} = 0 \qquad\qquad \text{on } \Gamma_{wall}, \tag{4.5}$$

$$\mathbf{u} = \mathbf{v} \qquad\qquad \text{on } \Gamma_{needle}, \tag{4.6}$$

$$-\frac{1}{\text{Re}} \boldsymbol{\nabla} \mathbf{u} \cdot \mathbf{n} + p\mathbf{n} = 0 \qquad\qquad \text{on } \Gamma_{sides}. \tag{4.7}$$

4.2   Numerical methods

The governing equations in section 4.1 are solved using the finite element software FreeFem++ [32]. This code programs the discrete equations derived from the finite element weak formulation of the problem presented in section 4.2.2 using a characteristic/Galerkin model to stabilize the convection terms. A straightforward implementation of the mesh moving scheme is presented in section 4.2.1.

4.2.1   ALE implementation on moving meshes

Different methods applied to predict flows in moving domains with the finite element method exist. Moving mesh methods use meshes following the domain occupied by the fluid. The mesh is then exactly given at the boundary. The ALE framework is mathematically rigorous to describe transport phenomena in time and allows some freedom in the description of the mesh motion. However, it raises some implementation questions on the interface tracking with time discretization. Implementation of the ALE method can be done in FreeFem++ [33].

In the present paper, the ALE framework in FreeFem++ is employed to compute the flow in the moving domain. In the current problem setting, the motion of needle is prescribed with respect to time. The boundary of the domain is thus exactly known at each time step so that an area preserving mesh can be precisely generated.

For a detailed description of the ALE approach, the readers can refer to [34]. The framework of the ALE approach is briefly described below. Let $\Omega(t)$ be the domain at each time t with regular boundary $\partial\Omega(t)$. In the Eulerian representation, the fluid is described by

$$\mathbf{u}(\mathbf{x}, t) \text{ and } p(\mathbf{x}, t), \forall \mathbf{x} \in \Omega(t). \tag{4.8}$$

To follow a moving domain, one can define the ALE map as

$$\tilde{\mathcal{A}} : \tilde{\omega} \times \mathbb{R}^+ \to \mathbb{R}^2 \quad (\tilde{\mathbf{x}}, t) \to \tilde{\mathcal{A}}(\tilde{\mathbf{x}}, t) := \tilde{\mathcal{A}}_t, \tag{4.9}$$

such that $\omega(t)=\tilde{\mathcal{A}}(\tilde{\omega},t)$, where $\tilde{\omega}$ is the reference computational domain. Given an ALE field $\tilde{q}:\tilde{\omega}\times\mathbb{R}^+\to\mathbb{R}$, its Eulerian description is given by

$$\forall\mathbf{x}\in\Omega(t),q(\mathbf{x},t)=\tilde{q}(\tilde{\mathcal{A}}_t^{-1}(\mathbf{x}),t) \tag{4.10}$$

In this framework, the computational domain velocity (ALE velocity or grid velocity) is defined as

$$\tilde{\mathbf{a}}(\tilde{\mathbf{x}},t)=\frac{\partial\tilde{\mathcal{A}}}{\partial t}(\tilde{\mathbf{x}},t),\quad\forall\tilde{\mathbf{x}}\in\tilde{\omega}, \tag{4.11}$$

so that we can get

$$\mathbf{a}(\mathbf{x},t)=\tilde{\mathbf{a}}(\tilde{\mathcal{A}}_t^{-1},t). \tag{4.12}$$

The ALE time-derivative is defined as

$$\left.\frac{\partial q}{\partial t}\right|_{\tilde{\mathcal{A}}}=\frac{\mathrm{d}}{\mathrm{d}t}q(\tilde{\mathcal{A}}(\tilde{\mathbf{x}},t),t), \tag{4.13}$$

and the following identity holds

$$\left.\frac{\partial q}{\partial t}\right|_{\tilde{\mathcal{A}}}=(\mathbf{a}.\boldsymbol{\nabla})q+\frac{\partial q}{\partial t}. \tag{4.14}$$

A general method used to construct the mapping, or equivalently the domain velocity $\mathbf{a}$, consists of solving the following equations

$$-\nabla^2\mathbf{a}+\nabla p=0, \tag{4.15}$$
$$\boldsymbol{\nabla}\cdot\mathbf{a}=0, \tag{4.16}$$
$$\mathbf{a}_{|_{\partial\Omega}}=\mathbf{f}. \tag{4.17}$$

In the ALE framework, subject to a prescribed needle motion (see figure 6), the equations (4.2-4.3) become

$$\frac{1}{\alpha_f}\left.\frac{\partial\mathbf{u}}{\partial t}\right|_{\tilde{\mathcal{A}}}-\frac{1}{\alpha_f}(\mathbf{a}\cdot\boldsymbol{\nabla})\mathbf{u}+\frac{1}{\alpha_f}\mathbf{u}\cdot\boldsymbol{\nabla}\left(\frac{\mathbf{u}}{\alpha_f}\right)-\frac{1}{\mathrm{Re}}\nabla^2\mathbf{u}+\frac{1}{\alpha_f}\boldsymbol{\nabla}(\alpha_f p)=-\frac{1}{\mathrm{DaRe}}\mathbf{u}, \tag{4.18}$$
$$\boldsymbol{\nabla}\cdot\mathbf{u}=0. \tag{4.19}$$

The solutions $\mathbf{u}$ and p are sought subject to the initial (3.4) and boundary conditions (3.5-3.7) described in section 4.1. The ALE time-derivative induces a correction term in the transport term by subtracting the computational domain velocity $\mathbf{a}$ from the transport velocity $\mathbf{u}$.

4.2.2 Finite element discretization

To solve for the convective Brinkman equations and to fix the pressure constant part, the convective Brinkman equations with the pseudo compressibility approximation are investigated

$$\frac{1}{\alpha_f}\frac{\partial \mathbf{u}}{\partial t}\bigg|_{\tilde{\mathcal{A}}} - \frac{1}{\alpha_f}(\mathbf{a}\cdot\boldsymbol{\nabla})\mathbf{u} + \frac{1}{\alpha_f}\mathbf{u}\cdot\boldsymbol{\nabla}\left(\frac{\mathbf{u}}{\alpha_f}\right) - \frac{1}{\mathrm{Re}}\nabla^2\mathbf{u} + \frac{1}{\alpha_f}\boldsymbol{\nabla}(\alpha_f p)$$

$$= -\frac{1}{\mathrm{DaRe}}\mathbf{u} \text{ in } \Omega(t), \tag{4.20}$$

$$\boldsymbol{\nabla}\cdot\mathbf{u} + \varepsilon p = 0 \text{ in } \Omega(t), \tag{4.21}$$

where ε is a small parameter. The formulation consisting of (4.20-4.21) follows the so called artificial compressibility method introduced in [35] and [36].

The convective Brinkman equations are approximated with the method of the characteristics for the nonlinear convection term and a Galerkin method for the rest of the spatial derivative terms. The time discretization of (4.20-4.21) gives

$$\frac{1}{\Delta t}\left(\frac{\mathbf{u}^{n+1}}{\alpha_f} - \left(\frac{\mathbf{u}^n}{\alpha_f}\right)\circ X^n(\mathbf{x})\right) - \frac{1}{\alpha_f}(\mathbf{a}\cdot\boldsymbol{\nabla})\mathbf{u}^{n+1} - \frac{1}{\mathrm{Re}}\nabla^2\mathbf{u}^{n+1}$$

$$+ \frac{1}{\alpha_f}\boldsymbol{\nabla}(\alpha_f p^{n+1}) = -\frac{1}{\mathrm{DaRe}}\mathbf{u}^{n+1} \text{ in } \Omega^{n+1}, \tag{4.22}$$

$$\boldsymbol{\nabla}\cdot\mathbf{u}^{n+1} + \varepsilon p^{n+1} = 0 \text{ in } \Omega^{n+1}. \tag{4.23}$$

Note that $X^n \approx \mathbf{x} - \frac{\mathbf{u}^n}{\alpha_f}(\mathbf{x})\Delta t$. For all $\varphi \in H^{1/2}(\Gamma_{\mathrm{needle}})$, let us introduce the product space

$$V_\varphi = \left\{ (\mathbf{w},q) \in [H^1(\Omega)]^2 \times L^2(\Omega), \mathbf{w} = \varphi \text{ on } \Gamma_{\mathrm{needle}}, \mathbf{w} = 0 \text{ on } \Gamma_{\mathrm{wall}} \right\}. \tag{4.24}$$

Let

$$(a,b) = \int_{\Omega^{n+1}} ab\,d\mathbf{x}. \tag{4.25}$$

From the weak form of (4.22 - 4.23) subject to the boundary conditions in (3.5 - 3.7), the time discretization gives the following scheme

$$\text{find } (\mathbf{u}^{n+1}, p^{n+1}) \in V_g \text{ such that}$$

$$\frac{1}{\Delta t}\left(\frac{\mathbf{u}^{n+1}}{\alpha_f} - \left(\frac{\mathbf{u}^n}{\alpha_f}\right)\circ X^n(\mathbf{x}), \mathbf{w}\right) - \left(\frac{1}{\alpha_f}(\mathbf{a}\cdot\boldsymbol{\nabla})\mathbf{u}^{n+1}, \mathbf{w}\right)$$

$$+ \frac{1}{\mathrm{Re}}\left(\frac{1}{\alpha_f}\boldsymbol{\nabla}\mathbf{u}^{n+1}, \boldsymbol{\nabla}\mathbf{w}\right) - \left(\alpha_f p^{n+1}, \boldsymbol{\nabla}\cdot\left(\frac{\mathbf{w}}{\alpha_f}\right)\right) + \frac{1}{\mathrm{DaRe}}\left(\mathbf{u}^{n+1}, \mathbf{w}\right) = 0, \tag{4.26}$$

$$\left(\boldsymbol{\nabla}\cdot\mathbf{u}^{n+1}, q\right) + \varepsilon\left(p^{n+1}, q\right) = 0, \tag{4.27}$$

$$\forall(\mathbf{w},q) \in V_0.$$

The Taylor-Hood P2–P1 elements are adopted to ensure satisfaction of the LBB (Ladyžhenskaya [37] - Babuška [38] - Brezzi [39]) stability condition. Note that temporal accuracy order of the presented characteristic/Galerkin method is one. The corresponding formulation for (4.26-4.27) at each time step is as follows within the framework of FreeFem++:

```
problem convbrinkmanEE([u1t,u2t,p],[v1,v2,q],solver=UMFPACK,init= iter) =
    int2d(Th)(
      (1./EEx/dt+ 1./Da/Re) * ( u1t * v1 + u2t *v2)
            + 1./Re/EEx* ( dx(u1t)*dx(v1) + dy(u1t)*dy(v1)
            +         dx(u2t)*dx(v2) + dy(u2t)*dy(v2) )
            + p*q*(0.00000000001)
            -p*dx(v1/EEx) - p*dy(v2/EEx)
            + dx(u1t)*q + dy(u2t)*q
          )
            -int2d(Th)((([-uEEx,-vEEx]'*[dx(u1t),dy(u1t)])*v1 )
  -int2d(Th)((([-uEEx,-vEEx]'*[dx(u2t),dy(u2t)])*v2 )
      + int2d(Th) (
  -1./dt*convect([u1EEx, u2EEx],-dt, u1EEx)*v1
  -1./dt*convect([u1EEx, u2EEx],-dt, u2EEx)*v2
  )
    + on(needle,u1t=u,u2t=v)
    + on(top,bottom,u1t=0,u2t=0);
```

Meshes are generated within FreeFem++ so that the solution is independent of the mesh. Mesh adaptation is performed prior to simulations so as to enhance the mesh quality around the needle and the cell.

5   Results and discussion

5.1   Effect of the needle motion on the interstitial flow

In this study, the needling direction is perpendicular to the skin surface. In practice, it is possible that the needling direction is oblique to the skin surface. The simulation results show that the insertion of an acupuncture needle can influence interstitial fluid flow. Indeed, under a stress field glycoproteins undergo fluidization. The computed velocity field shows that the magnitude of the velocity is higher in regions close to the needle tip (figure 3) and quickly it can vanish at a location away from the needle due to repolymerization of glycoprotein constituents.

Furthermore, when the needle reaches its maximum speed, the interstitial pressure gradient becomes higher at a location close to the needle tip (figure 4). The changes in the interstitial fluid flow and the high pressure gradient can affect the activities of the mastocyte pools in the stimulated area.

5.2 Effects of the fractional fluid volume and the Darcy permeability on the interstitial flow

The fractional fluid volume α_f, defined in equation (3.3), and the Darcy permeability $\mathcal{P}$ are chosen to model the fibrous tissue matrix. It is noted that the fractional fluid volume and the permeability alone cannot fully describe the microscopic behavior of the fiber matrix. Acupoints are situated in regions, close to neurovascular bundles, in which fibrous matrix, capillaries, lymphatic vessels, nervous structures, and cells abound. It is then reasonable to make the assumption that the fractional fluid volume α_f is lower at the acupoint loci. In soft tissues, the permeability of the tissue $\mathcal{P}$ varies with the fluid volume fraction α_f [18]. Amongst the laws for the permeability of the tissue reported in [40], the Karman-Kozeny relation given in [41] is adopdted. The Karman-Kozeny equation relates the permeability $\mathcal{P}$ to the fractional fluid volume α_f and the extracellular matrix fiber properties. With a simplified and structured network of cylindrical parallel and perpendicular fibers, the Karman-Kozeny equation reads as follows [18]

$$\mathcal{P} = \frac{\alpha_f f_r^2}{f_k} \tag{5.1}$$

where $f_r = (f_s^2 - f_d^2)/4f_d$ and $f_k = (2/3)k_+ + (1/3)k_-$. Note that f_d and f_s correspond to the fiber diameter and the fiber spacing, respectively.

$$k_+ = 2\alpha_f^3/(1-\alpha_f)\left[\ln(1/(1-\alpha_f)) - (1-(1-\alpha_f)^2)/(1+(1-\alpha_f)^2)\right]$$

and

$$k_- = 2\alpha_f^3/(1-\alpha_f)\left[2\ln(1/(1-\alpha_f)) - 3 + 4(1-\alpha_f) - (1-\alpha_f)^2\right]$$

model the resistance to a flow perpendicular and parallel to the fibers, respectively. The flow through interstitium is computed according to the data given in [40]. The simulation results shown in figure 6 suggest that the effects of the needle on the interstitial pressure are more effective in a fiber richer tissue. In particular, the expected high interstitial pressure is achieved only at acupoint.

Another case to consider is the local decrease of the values α_f and $\mathcal{P}$ such that they reach their minimum precisely at the acupoint. The simulation results reveal that a proper location of the insertion of the needle is relevant. The effects of the needle on the interstitial flow are greater when the needle is inserted exactly at the acupoint. According to the α_f and $\mathcal{P}$ distributions on the one hand and to the needle position with respect to the location of the peak density of fibers (figures 6(a), 6(b), and 6(c)) on the other hand, the expected high pressure solution is reached only when the needle is inserted at the acupoint (figure 6).

5.3 Shear stress and pressure distribution along the cell membrane

In this section we are interested in the effects of the fluidic stimuli on a interstitial cell. Simulations are carried out by considering no-slip boundary condition prescribed at the

cell surface. Figure 7 shows the velocity magnitude and the pressure contours with a cell added closely to the needle.

Figure 8 shows the distribution of the shear stress and the pressure along the cell surface. The cell is mapped to the trigonometric unit circle, where θ denotes the angle in radian. The pressure on the cell surface is higher at a point closest to the needle tip ($\theta \in \left[\frac{\pi}{2}, \frac{3\pi}{2}\right]$), whereas the shear stress can be higher on the side furthest from the needle ($\theta \in \left[-\frac{3\pi}{2}, \frac{\pi}{2}\right]$). The interstitial flow induced by needle motion leads to a phase shift around the cell surface of the maximum shear stress and pressure value. This shows that all the cell surface could be stimulated.

Mastocytes have been shown to respond to fluid shear stress [42]. These local mechanical forces can trigger the activation of mechanoresponsive proteins on the cell surface [11] so that Ca^{++} is allowed to enter the cytosol via pressure and shear stress gated ion channels.

6   Concluding remarks

Insertion into the skin of a thin needle is the most common acupuncture technique. The insertion of a needle generates a mechanical stress field in the interstitium. In the present study, the deformation of the extracellular matrix is neglected and only the effect of interstitial flow is considered.

The simulation results suggest that the needling effects are most effective when an accurate insertion and a manipulation are exerted. High local fluid pressure and shear stress on cells are most likely to appear near the needling region. Fluidic stimuli can contribute to the mastocyte activation via sensory transduction that is immediately followed by granule exocytosis.

A self-sustained process is created via the recruitment of regional and circulating mastocytes [10, 11]. Newly recruited mastocytes at acupoints experience a degranulation triggered by the stress field. This process enhances vascular and endocrine signaling that supports a delayed and permanent response from the central nervous system [11].

Clearly, numerical prediction of the interstitial pressure and shear stress is an essential tool to gain a better understanding of the mechanism involved in the acupuncture needling.
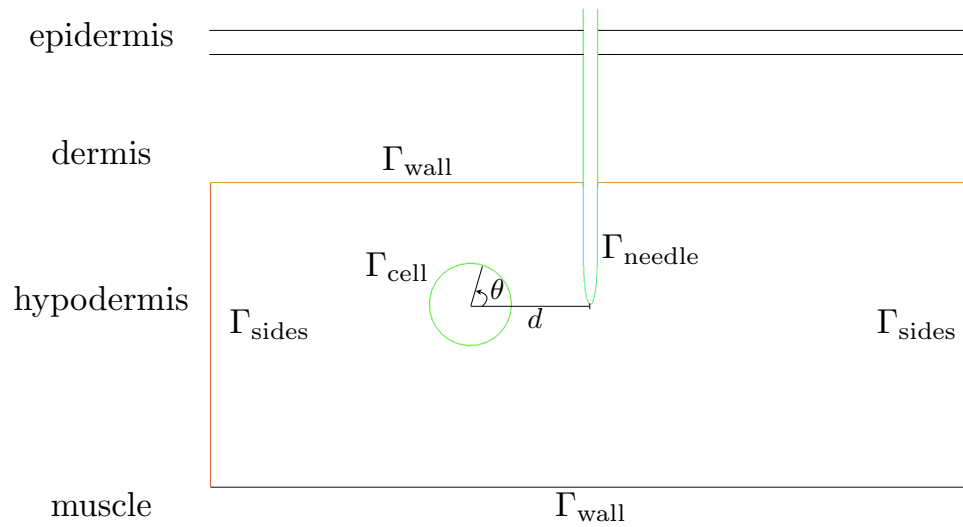
Figure 1: Schematic of the computational domain Ω. The cell is mapped to the trigonometric unit circle where θ, in radian, is the angle. d is the distance along the x-axis between the cell center and the needle tip.
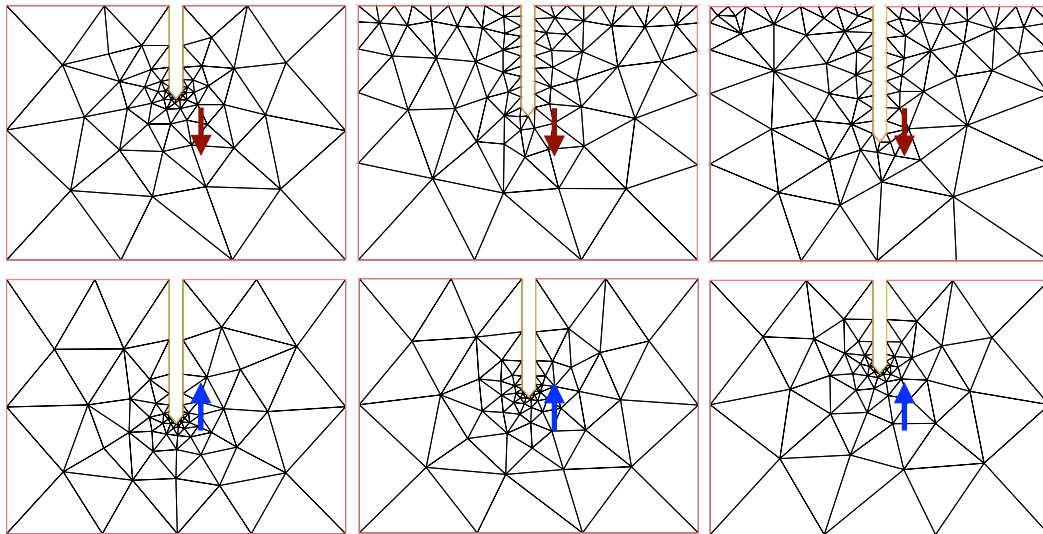

Figure 2: Illustration of the prescribed moving needle motion and the generated meshes (not actual meshes). At each time step, the new mesh is generated by the FreeFem++ **movemesh** function.
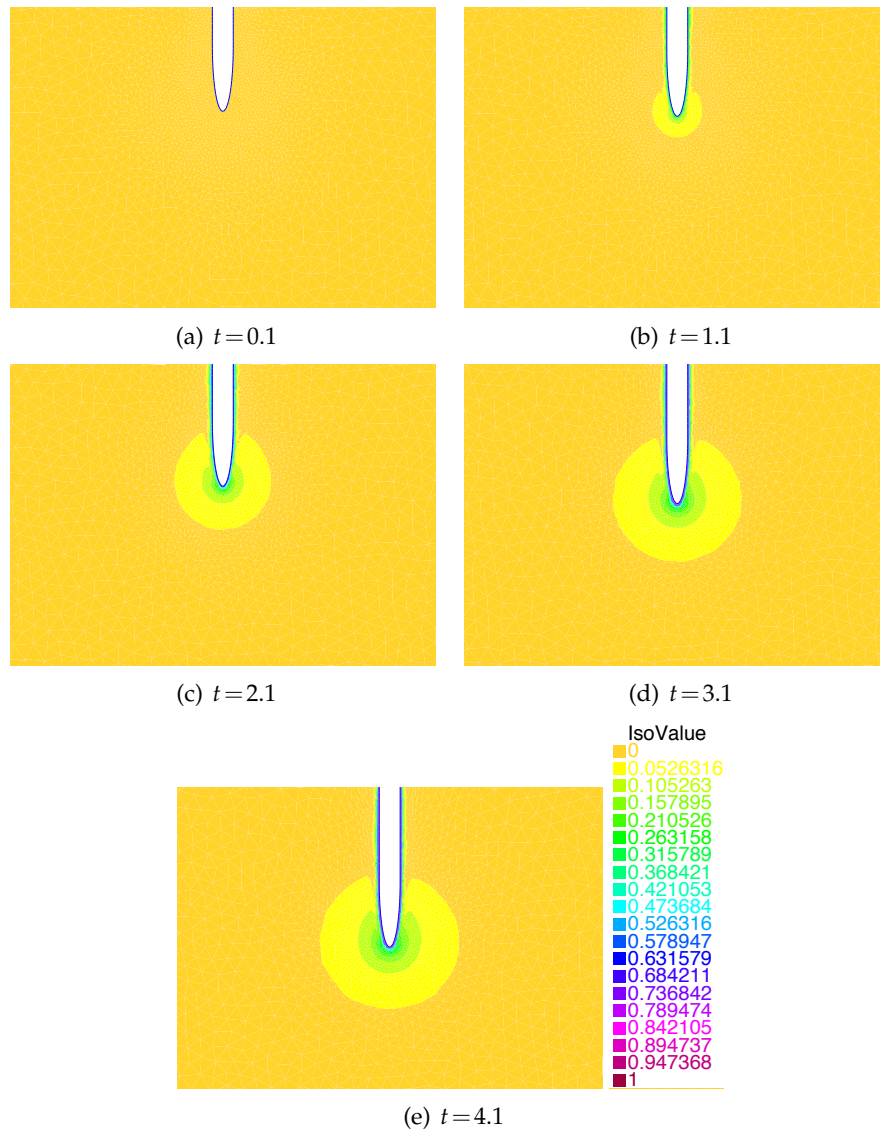
(a) $t=0.1$

(b) $t=1.1$

(c) $t=2.1$

(d) $t=3.1$

(e) $t=4.1$

Figure 3: The predicted time varying velocity magnitude $|\mathbf{u}|$ resulting from the needle motion in interstitial fluid.
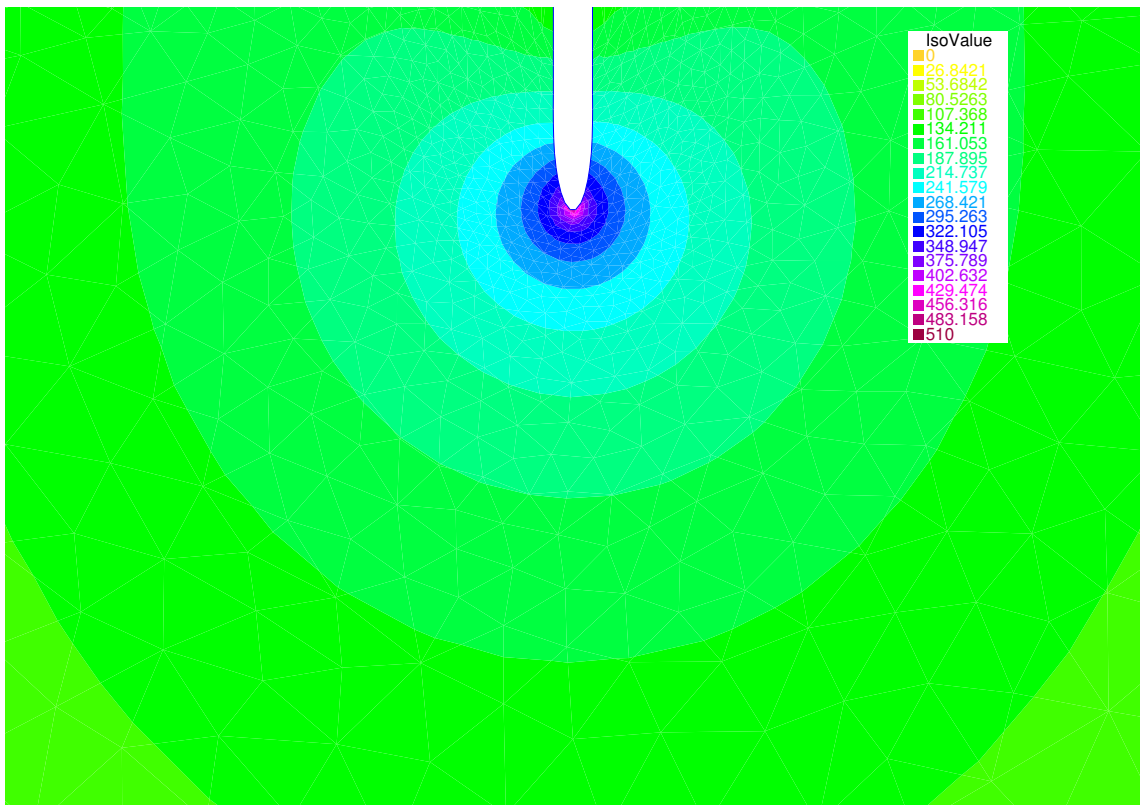
(a) $t=0.1$

(b) $t=1.1$

(c) $t=2.1$

(d) $t=3.1$

IsoValue
0
25052.6
50105.3
75157.9
100211
125263
150316
175368
200421
225474
250526
275579
300632
325684
350737
375789
400842
425895
450947
476000

(e) $t=4.1$
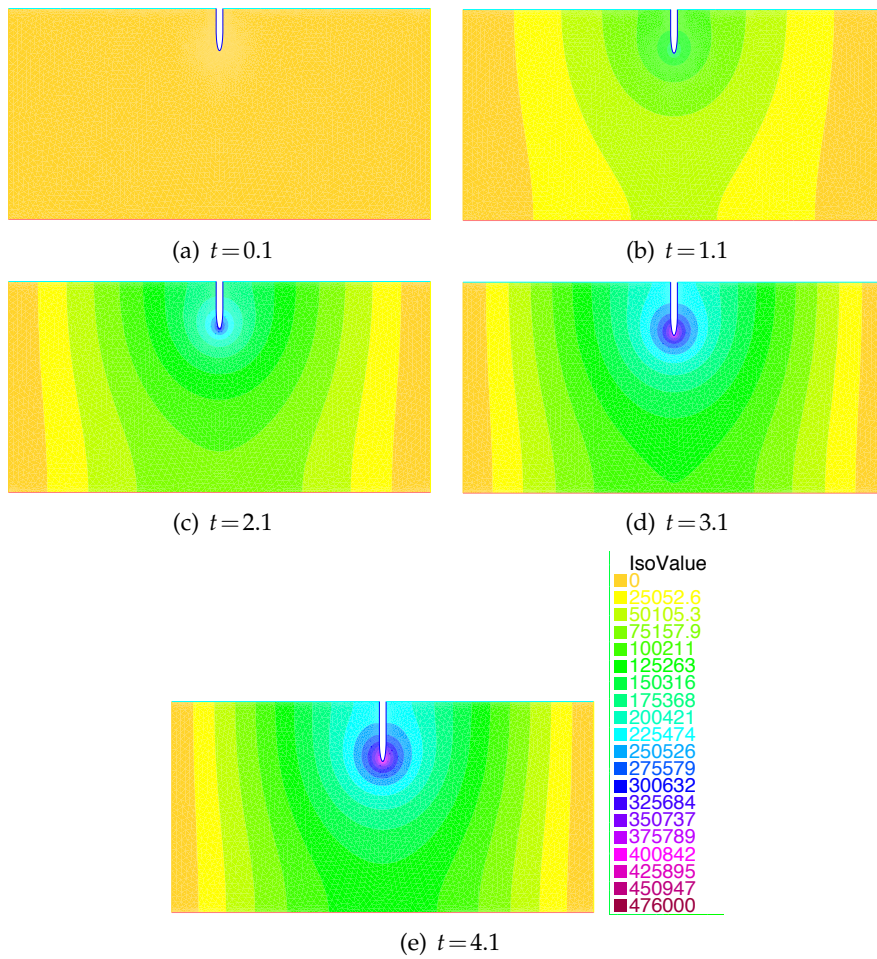
Figure 4: The predicted time varying pressure contours resulting from the needle motion in interstitial fluid.
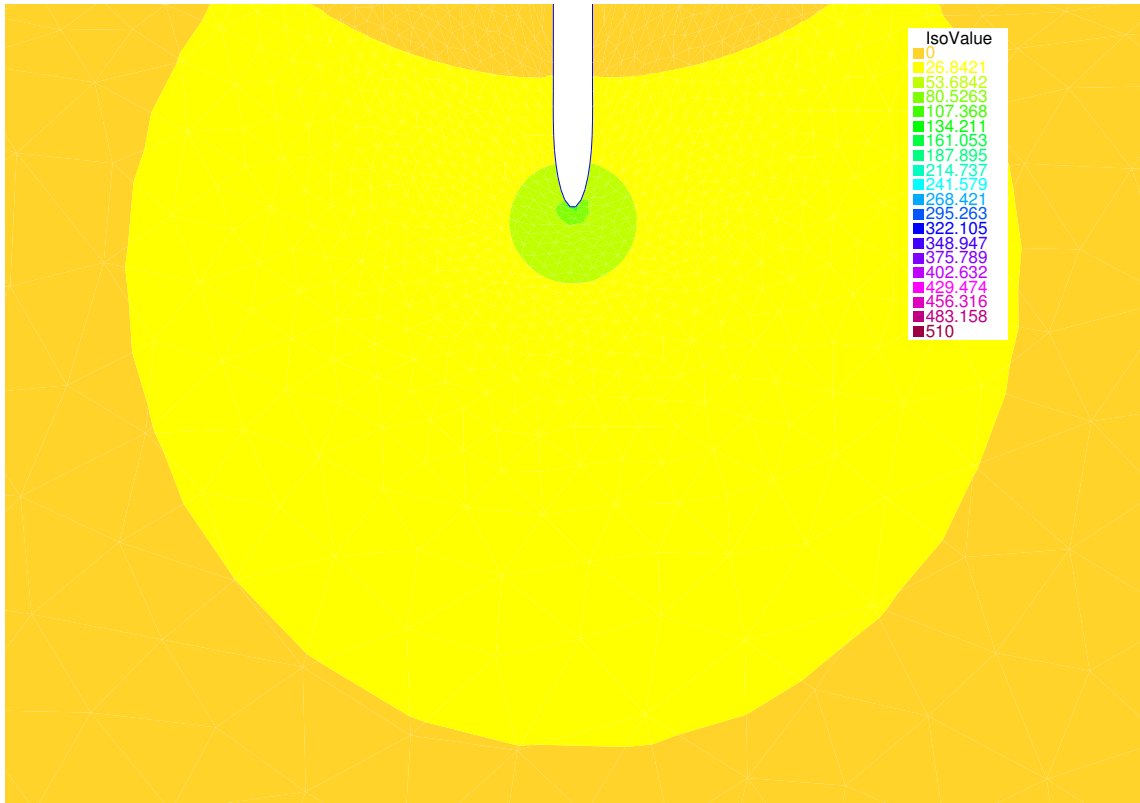
(a) $\alpha_f = 0.7$, Da $= 0.321$, Re $= 0.103$

(b) $\alpha_f = 0.6$ Da $= 0.040$, Re $= 0.103$

Figure 5: The predicted pressure contours resulting from the motion of a needle in interstitial fluid of the subcutaneous connective tissue at acupoint (b) and in a non-acupoint (a). High interstitial pressure is only expected to occur at acupoint.

(a) α_f distribution with needle at acupoint.

(b) α_f distribution with needle close to acupoint.

(c) α_f distribution with needle far from acupoint.
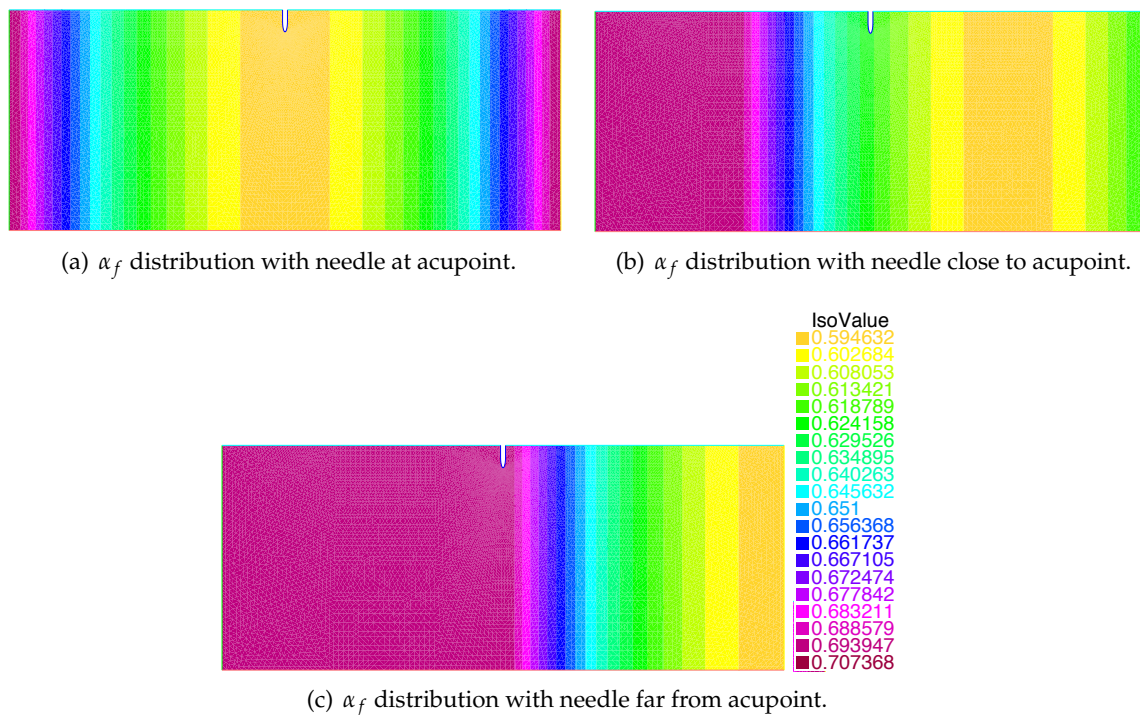
(d) Pressure p resulting from the motion of the needle at different locations.

Figure 6: The predicted contours of α_f. Regions with a lower magnitude of α_f correspond to regions where the fibrous medium is denser. The needle is inserted (a) at the acupoint, (b) close to the acupoint, and (c) far from the acupoint. On each numerical experiment, the needle is inserted at the same coordinate while the α_f distribution is shifted. (d) High interstitial pressure is only expected to occur when the needle, displayed by the dot lines, is inserted at acupoint.
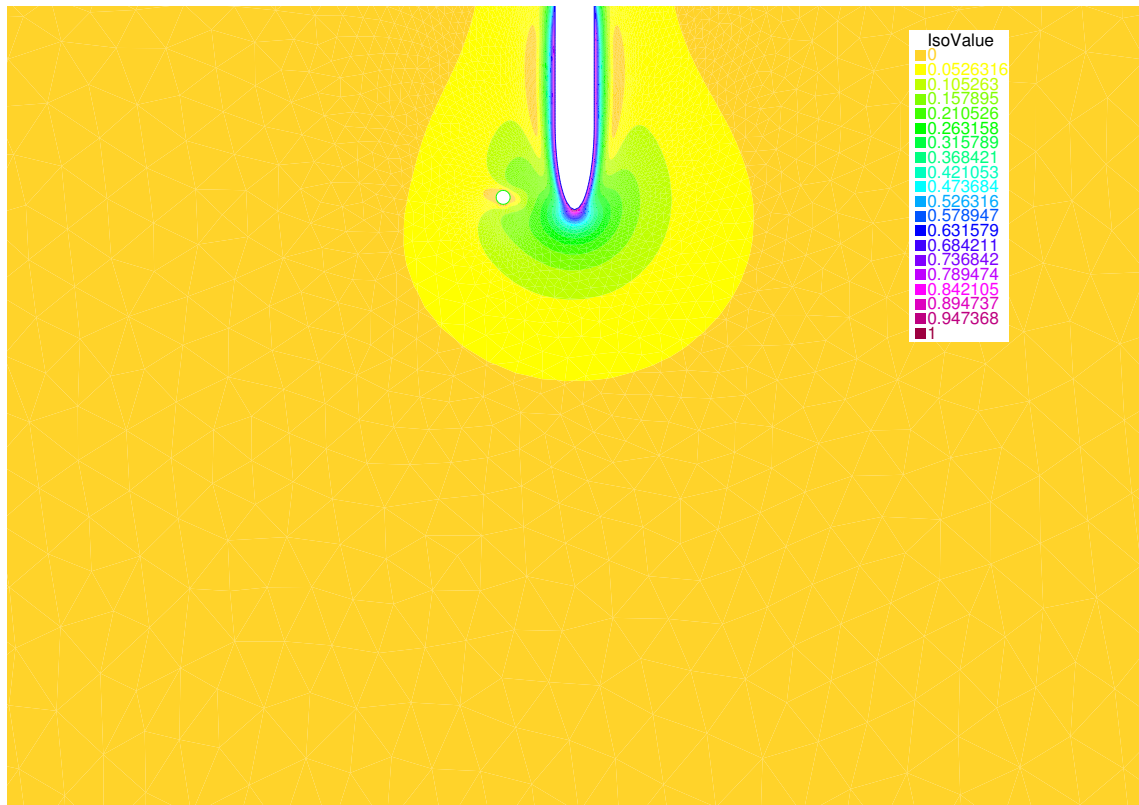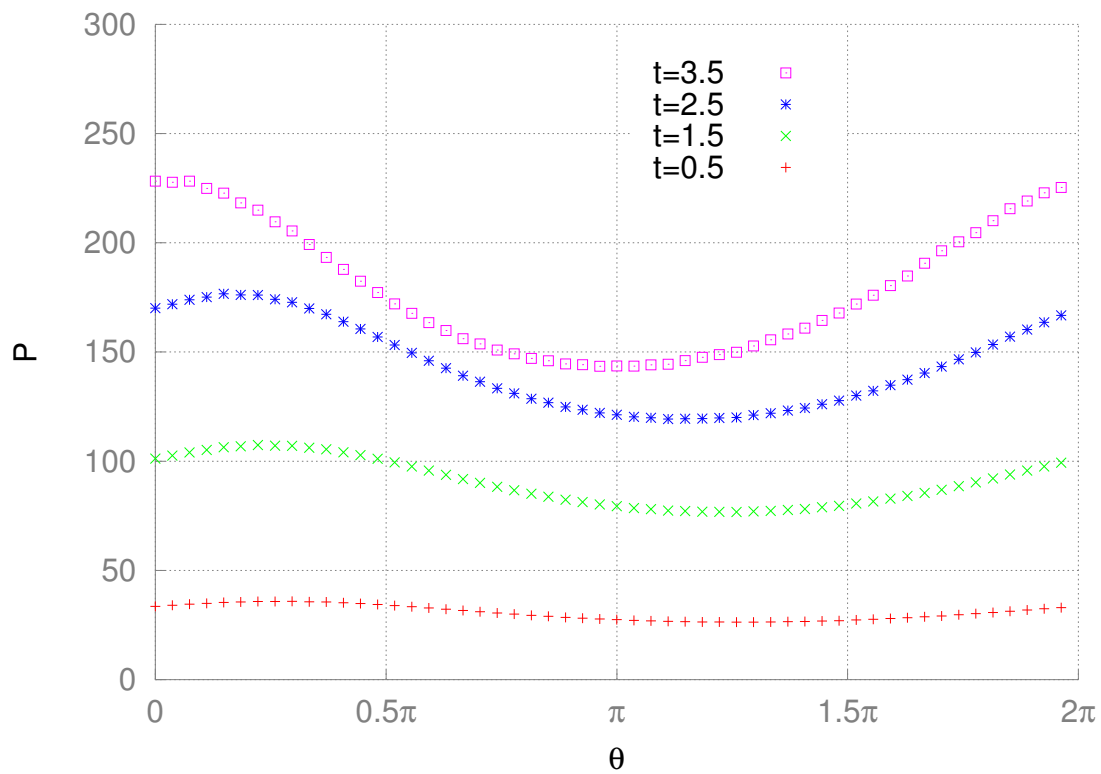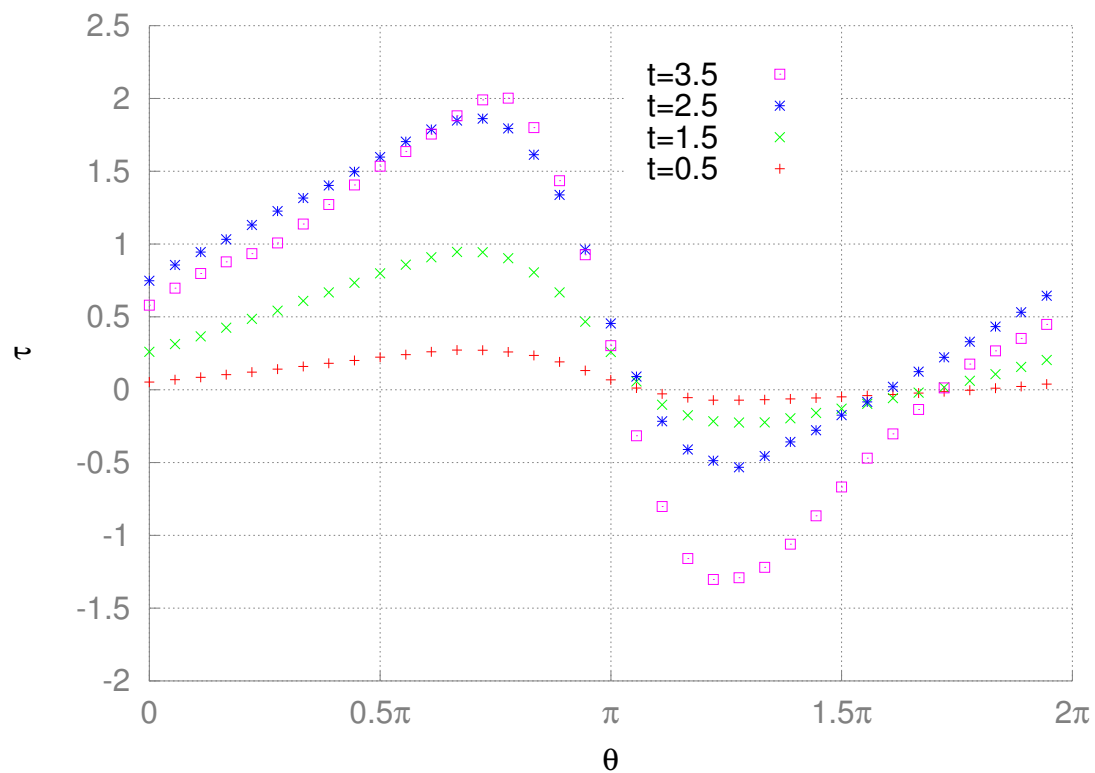
(a)
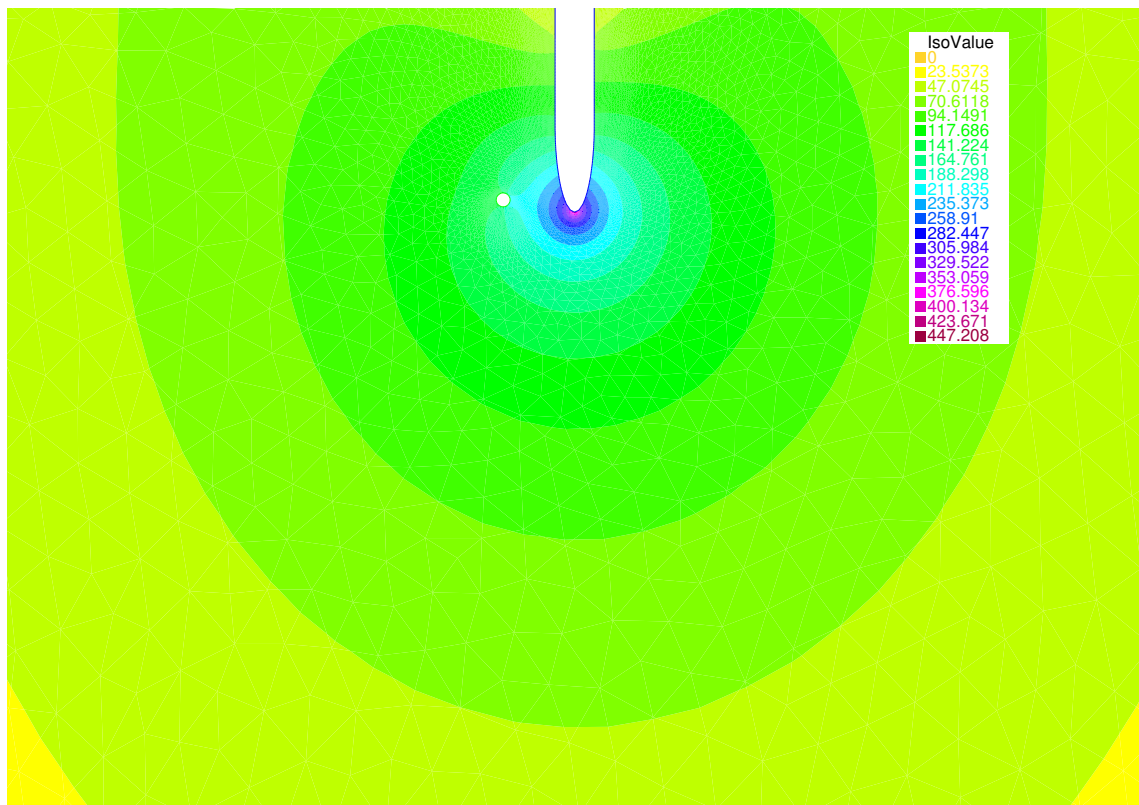
(b)

Figure 7: The predicted contours of (a) the velocity and (b) the pressure with an interstitial cell inserted at a location near the needle.
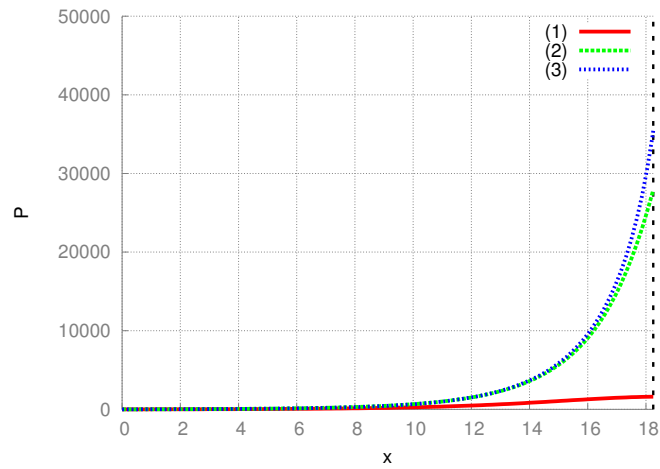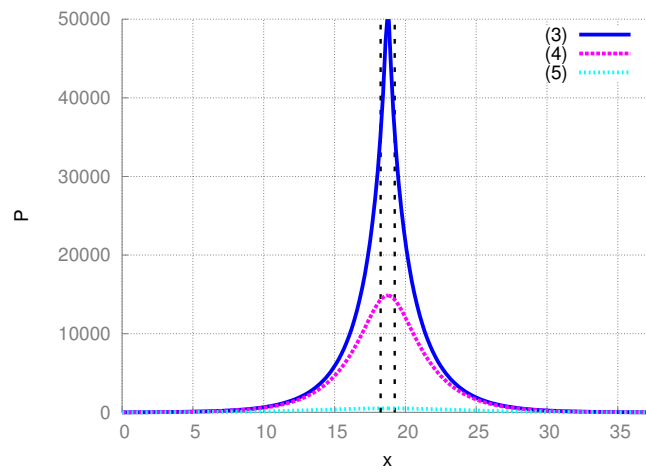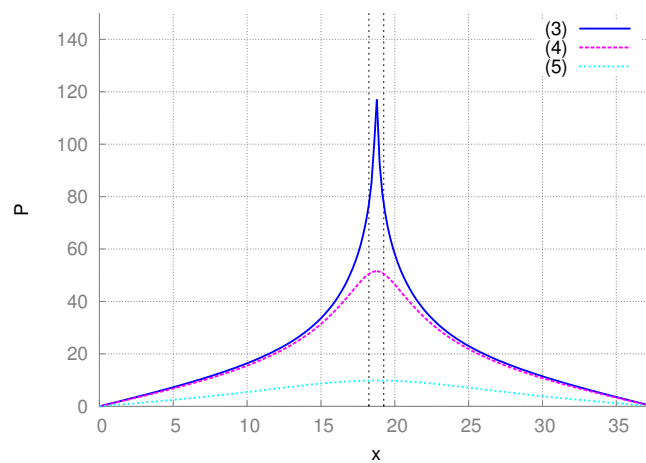
(a)

(b)

Figure 8: Evolution of (a) the pressure and (b) the shear stress distributions along the cell surface. The cell is mapped to the trigonometric unit circle where θ, in radian, is the angle defined in figure 1.

(a) Convective Brinkman: $\mathrm{Re}=0.208$, $\mathrm{Da}=3.48\times10^{-05}$, $\alpha_f=0.6$.

(b) Convective Brinkman: $\mathrm{Re}=0.208$, $\mathrm{Da}=3.48\times10^{-05}$, $\alpha_f=0.6$.

(c) Navier-Stokes: $\mathrm{Re}=0.208$.

Figure 9: The simulated pressures p at different vertical locations: (1) at half the height of the needle, (2) the middle of the needle tip, (3) the needle tip, at (4) half the height of the needle tip under the needle, and (5) half the height between the needle tip and the bottom wall. The lines in dots show the x-position of the needle.
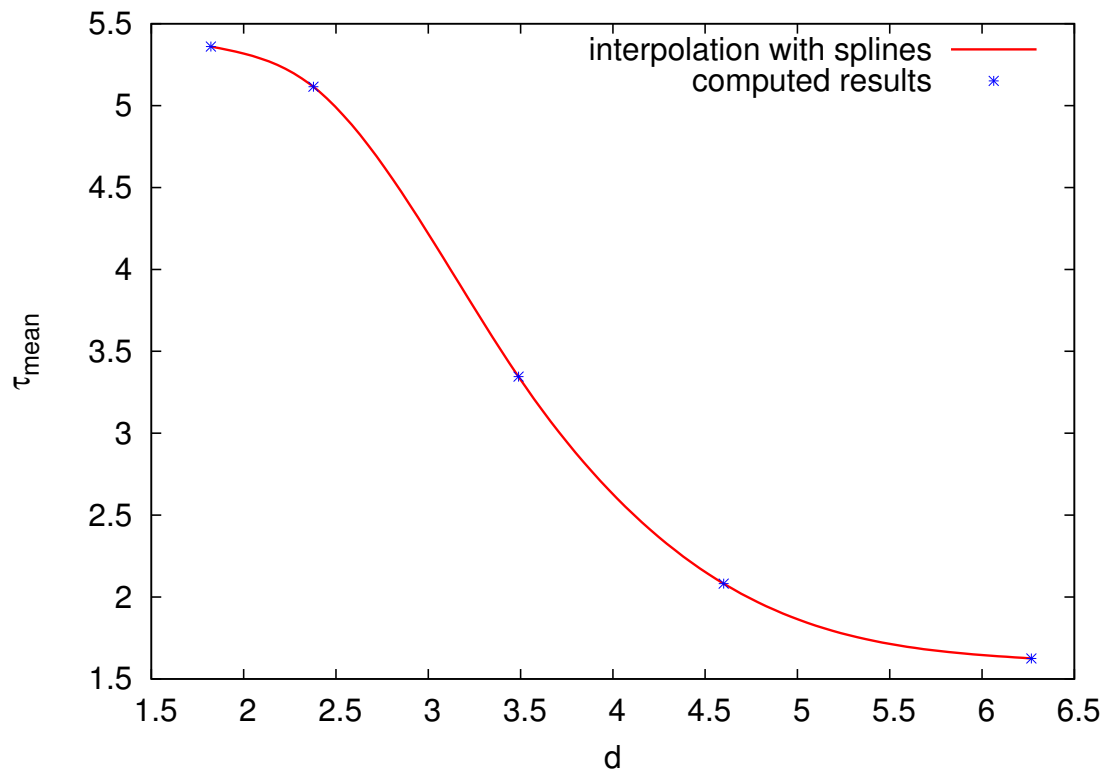
Figure 10: The predicted mean shear stress τ_{mean} on the cell surface with respect to the distance d measured from the needle (see figure 1). A higher shear stress is expected to be observed at a location close to the needle.

References

[1] X. Cheng, *Chinese Acupuncture and Moxibustion*. Beijing: Foreign Language Press, 1st ed. ed., 1987.

[2] H. M. Langevin, D. L. Churchill, J. R. Fox, G. J. Badger, B. S. Garra, and M. H. Krag, "Biomechanical response to acupuncture needling in humans," *Journal of Applied Physiology*, vol. 91, no. 6, pp. 2471–2478, 2001.

[3] D. Zhang, G. Ding, X. Shen, W. Yao, Z. Zhang, Y. Zhang, J. Lin, and Q. Gu, "Role of mast cells in acupuncture effect: a pilot study," *Explore (New York, N.Y.)*, vol. 4, no. 3, pp. 170–177, 2008.

[4] G. A. Ulett, S. Han, and J.-s. Han, "Electroacupuncture: mechanisms and clinical application," *Biological Psychiatry*, vol. 44, pp. 129–138, July 1998.

[5] P. Whittaker, "Laser acupuncture: past, present, and future," *Lasers in Medical Science*, vol. 19, pp. 69–80, Oct. 2004.

[6] C. Huang and T. W. Sheu, "Study of the effect of moxibustion on the blood flow," *International Journal of Heat and Mass Transfer*, vol. 63, pp. 141–149, 2013.

[7] V. C. Huang and T. W. H. Sheu, "Heat transfer involved in a warm (moxa-heated) needle treatment," *Acupuncture & Electro-Therapeutics Research*, vol. 33, no. 3-4, pp. 169–178, 2008.

[8] V. C. Huang and T. W. H. Sheu, "On a dynamical view on the meridian transmission," *Journal of Accord Integrative Medicine*, vol. 4, no. 2, 2008.

[9] V. C. Huang and T. W. H. Sheu, "Tissue fluids in microchannel subjected to an externally applied electric potential," *International Journal of Numerical Methods for Heat & Fluid Flow*, vol. 19, no. 1, pp. 64–77, 2009.

[10] Y. Deleuze, "A mathematical model of mast cell response to acupuncture needling," *Comptes Rendus Mathematique*, vol. 351, no. 3-4, pp. 101–105, 2013.

[11] M. Thiriet, *Intracellular Signaling Mediators in the Circulatory and Ventilatory Systems*, vol. 4 of *Biomathematical and Biomechanical Modeling of the Circulatory and Ventilatory Systems*. New York, NY: Springer New York, 2013.

[12] M. Thiriet, Y. Deleuze, and T. W. H. Sheu, "A biological model of acupuncture and its derived mathematical modeling and simulations," *Communications in Computational Physics*, 2015.

[13] M. Thiriet, *Biology and mechanics of blood flows: Part I: Biology*. CRM Series in Mathematical Physics, Springer, NY, 2008.

[14] M. Thiriet, "Cells and tissues," in *Cell and Tissue Organization in the Circulatory and Ventilatory Systems*, no. 1 in Biomathematical and Biomechanical Modeling of the Circulatory and Ventilatory Systems, pp. 11–67, Springer New York, Jan. 2011.

[15] P. Fung, "Probing the mystery of Chinese medicine meridian channels with special emphasis on the connective tissue interstitial fluid system, mechanotransduction, cells durotaxis and mast cell degranulation," *Chinese Medicine*, vol. 4, no. 1, p. 10, 2009.

[16] J. A. Pedersen, F. Boschetti, and M. A. Swartz, "Effects of extracellular fiber architecture on cell membrane shear stress in a 3D fibrous matrix," *Journal of Biomechanics*, vol. 40, no. 7, pp. 1484–1492, 2007.

[17] A. Blasselle, *Modélisation mathématique de la peau*. Thèse de doctorat, Université Pierre et Marie Curie, Paris, France, 2011.

[18] M. A. Swartz and M. E. Fleury, "Interstitial flow and its effects in soft tissues," *Annual Review of Biomedical Engineering*, vol. 9, no. 1, pp. 229–256, 2007.

[19] H. C. Brinkman, "A calculation of the viscous force exerted by a flowing fluid on a dense

swarm of particles," *Applied Scientific Research*, vol. 1, pp. 27–34, Dec. 1949.

[20] M. Thiriet, *Cell and Tissue Organization in the Circulatory and Ventilatory Systems*, vol. 1 of *Biomathematical and Biomechanical Modeling of the Circulatory and Ventilatory Systems*. New York, NY: Springer New York, 2011.

[21] M. Biot, "Theory of finite deformations of porous solids," *Indiana University Mathematics Journal*, vol. 21, no. 7, pp. 597–620, 1972.

[22] M. A. Biot, "General theory of three–dimensional consolidation," *Journal of Applied Physics*, vol. 12, no. 2, pp. 155–164, 1941.

[23] M. A. Biot, "Theory of elasticity and consolidation for a porous anisotropic solid," *Journal of Applied Physics*, vol. 26, no. 2, pp. 182–185, 1955.

[24] M. A. Biot, "Mechanics of deformation and acoustic propagation in porous media," *Journal of Applied Physics*, vol. 33, no. 4, pp. 1482–1498, 1962.

[25] W. Yao and G. H. Ding, "Interstitial fluid flow: simulation of mechanical environment of cells in the interosseous membrane," *Acta Mechanica Sinica*, vol. 27, pp. 602–610, Aug. 2011.

[26] W. Yao, Y. Li, and G. Ding, "Interstitial fluid flow: The mechanical environment of cells and foundation of meridians," *Evidence-Based Complementary and Alternative Medicine*, vol. 2012, pp. 1–9, 2012.

[27] J. Y. Park, S. J. Yoo, L. Patel, S. H. Lee, and S.-H. Lee, "Cell morphological response to low shear stress in a two-dimensional culture microsystem with magnitudes comparable to interstitial shear stress," *Biorheology*, vol. 47, pp. 165–178, Jan. 2010.

[28] P. Forchheimer, "Wasserbewegung durch boden," *Z. Ver. Deutsch. Ing*, vol. 45, no. 1782, p. 1788, 1901.

[29] C. T. Hsu and P. Cheng, "Thermal dispersion in a porous medium," *International Journal of Heat and Mass Transfer*, vol. 33, pp. 1587–1597, Aug. 1990.

[30] P. Nithiarasu, K. N. Seetharamu, and T. Sundararajan, "Natural convective heat transfer in a fluid saturated variable porosity medium," *International Journal of Heat and Mass Transfer*, vol. 40, pp. 3955–3967, Oct. 1997.

[31] K. Vafai and C. L. Tien, "Boundary and inertia effects on flow and heat transfer in porous media," *International Journal of Heat and Mass Transfer*, vol. 24, pp. 195–203, Feb. 1981.

[32] F. Hecht, "New development in FreeFem++," *Journal of Numerical Mathematics*, vol. 20, no. 3-4, p. 251, 2013.

[33] Decoene A. and Maury B., "Moving meshes with FreeFem++," *Journal of Numerical Mathematics*, vol. 20, p. 195, 2013.

[34] M. A. Fernández, L. Formaggia, J.-F. Gerbeau, and A. Quarteroni, "The derivation of the equations for fluids and structure," in *Cardiovascular Mathematics* (L. Formaggia, A. Quarteroni, and A. Veneziani, eds.), no. 1 in MS&A, pp. 77–121, Springer Milan, Jan. 2009.

[35] A. J. Chorin, "A numerical method for solving incompressible viscous flow problems," *Journal of Computational Physics*, vol. 2, pp. 12–26, Aug. 1967.

[36] R. Témam, "Une méthode d'approximation de la solution des équations de Navier-Stokes," *Bulletin de la Société Mathématique de France*, vol. 96, pp. 115–152, 1968.

[37] O. A. Ladyženskaja, *The mathematical theory of viscous incompressible flow*. New York: Gordon and Breach Science, 1969.

[38] P. I. Babuška, "Error-bounds for finite element method," *Numerische Mathematik*, vol. 16, pp. 322–333, Jan. 1971.

[39] F. Brezzi, "On the existence, uniqueness and approximation of saddle-point problems arising from Lagrangian multipliers," *ESAIM: Mathematical Modelling and Numerical Analysis - Modélisation Mathématique et Analyse Numérique*, vol. 8, no. R2, pp. 129–151, 1974.

[40] J. R. Levick, "Flow through interstitium and other fibrous matrices," *Experimental Physiology*, vol. 72, pp. 409–437, Oct. 1987.

[41] J. Happel, "Viscous flow relative to arrays of cylinders," *AIChE Journal*, vol. 5, pp. 174–177, June 1959.

[42] F. Wei, X. Shi, J. Chen, and L. Zhou, "Fluid shear stress-induced cytosolic calcium signaling and degranulation dynamics in mast cells," *Cell Biology International Reports*, 2012.